

Robust Subspace Recovery Layer for Unsupervised Anomaly Detection

Chieh-Hsin Lai^{*1}, Dongmian Zou^{*2}, and Gilad Lerman¹

¹School of Mathematics

²Institute for Mathematics and its Applications
University of Minnesota, Minneapolis, MN 55455
{laixx313, dzou, lerman}@umn.edu

Abstract

We propose a neural network for unsupervised anomaly detection with a novel robust subspace recovery layer (RSR layer). This layer seeks to extract the underlying subspace from a latent representation of the given data and remove outliers that lie away from this subspace. It is used together with an encoder and a decoder. The encoder maps the data into the latent space, from which the RSR layer extracts the subspace. The decoder then smoothly maps back the underlying subspace to a “manifold” close to the original data. We illustrate algorithmic choices and performance for artificial data with corrupted manifold structure. We also demonstrate competitive precision and recall for image datasets.

1. Introduction

Finding and utilizing patterns in visual data is a common task for computer vision systems. However, there is often some anomalous visual information that does not follow a common pattern. Anomaly detection, that is, identifying data points that “do not conform to expected behavior” [1], is thus an important task. In many computer vision applications, there is no ground truth available to distinguish anomalous images from normal images. Thus anomalous images need to be detected in an unsupervised fashion. For example, one may need to remove anomalous images from a set of images obtained by a search engine without any prior knowledge about how a normal image should look [2]. Similarly, one may need to remove anomalous frames from a video obtained by a camera without any prior knowledge on normal frames [3]. In these examples, the only assumptions are that normal data points appear more often than anomalous ones and have a simple underlying structure which is

^{*}Equal contribution.

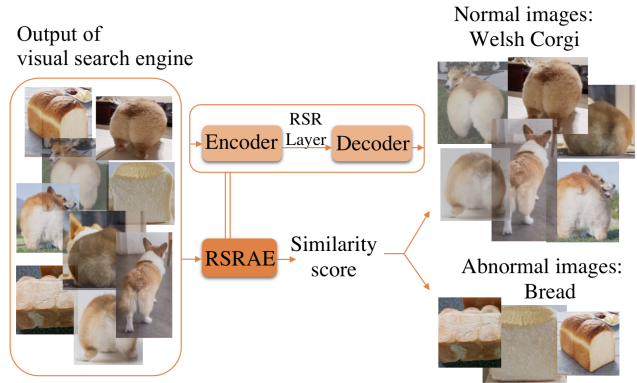


Figure 1: Demonstration of RSRAE for anomaly detection using a set of images obtained by a visual search engine.

unknown to the user.

Some early methods for anomaly detection relied on Principal Component Analysis (PCA) [4]. Here one assumes that the underlying unknown structure of the normal samples is linear. However, PCA is sensitive to anomalousities and will often not succeed in recovering the linear structure or identifying the outliers [5, 6]. More recent ideas of Robust PCA (RPCA) [6, 7] have been considered for some specific problems of anomaly detection or removal [8, 9]. RPCA assumes sparse corruption, that is, few elements of an image set or frames of a video are corrupted. This assumption is natural for some special problems in computer vision, in particular, background subtraction [6, 7, 10]. However, a natural setting of anomaly detection with hidden linear structure may assume that a large portion of the data points are fully corrupted. In this case the whole data matrix is not sparsely corrupted. The mathematical framework that addresses this setting is referred to as robust subspace recovery (RSR) [5].

While Robust PCA and RSR try to extract linear struc-

ture or identify outliers lying away from such structure, the underlying geometric structure of many real datasets is nonlinear. Therefore, one needs to extract crucial features of the nonlinear structure of the data while being robust to outliers. In order to achieve this goal, we propose to use an autoencoder (composed of an encoder and a decoder) with an RSR layer. We refer to it as RSRAE (RSR autoencoder). Fig. 1 illustrates the general structure of RSRAE. It aims to robustly and nonlinearly reduce the dimension of the data in the following way. The encoder first maps the data into a high-dimensional space, unlike a normal encoder that maps the data into a low-dimensional space. The enforced RSR layer plays a role in learning the hidden low-dimensional linear structure of the embedded normal data points. The decoder maps the data from this robust low-dimensional subspace back to a “manifold” sufficiently close to the original dataset.

Ideally, the encoder maps the normal data to a linear space and any anomalies lie away from this subspace. In this ideal scenario, anomalies can be removed by an RSR method directly applied to the data embedded by the encoder. Since the linear model for the normal data embedded by the encoder is only approximate, we do not directly apply RSR to the embedded data. Instead, we minimize a sum of the reconstruction error of the autoencoder and the RSR error for the data embedded by the encoder. We apply an alternating procedure, so that the parameters of the three different components (encoder, RSR layer and decoder) are optimized in turn.

We next review works that are directly related to this simple procedure. We then highlight the original contributions of this paper and describe the structure of the rest of the paper.

1.1. Related works

Several recent works have used autoencoders for anomaly detection. Autoencoders tend to maintain the main structure in the data and often produce large reconstruction errors for outliers, which help identify them. The earliest work on anomaly detection by large reconstruction error of an autoencoder is [2]. It applies an iterative and cyclic scheme, where in each iteration, an inlier set is determined and used for updating the parameters of the autoencoder. Aytekin et al. [11] apply ℓ_2 normalization for the latent code of the autoencoder and also consider the case of multiple modes for the normal samples. Instead of using the reconstruction error, they apply k -means clustering for the latent code, and identify outliers as points whose latent representations are far from all the cluster centers. Zhong et al. [12] also use an autoencoder with clustered latent code, but they fit a Gaussian Mixture Model using an additional neural network. Restricted Boltzmann Machines (RBMs) are similar to autoencoders. Zhai et al. [13] define “energy functions”

for RBMs that are similar to the reconstruction losses for autoencoders. They identify anomalous samples according to large energy values.

The above works are designed for datasets with a small fraction of outliers. However, when this fraction increases, outliers are often not distinguished by high reconstruction errors or low similarity scores. In order to identify them, additional assumptions on the structure of the normal data need to be incorporated. For example, Zhou and Paffenroth [8] decompose the input data into two parts: low-rank and sparse (or column-sparse). The low-rank part is fed into an autoencoder and the sparse part is imposed as a penalty term with the ℓ_1 -norm (or $\ell_{2,1}$ -norm for column-sparsity).

In this work, we use a term analogous to the $\ell_{2,1}$ -norm. This term can be interpreted as the sum of absolute deviations from a latent subspace. However, we do not decompose the data a priori, but minimize an energy combining this term and the reconstruction error. Minimization of the single term is known as least absolute deviations in RSR [5]. This energy is rotation invariant and its minimization was first suggested for RSR and related problems in [14, 15, 16]. The robustness to outliers of this energy, or of relaxed versions of it, was studied in [17, 18, 19, 20, 21, 22, 23]. In particular, Maunu et al. [23] established its well-behaved landscape under special, though natural, deterministic conditions. Under similar conditions, they guaranteed fast subspace recovery by a simple algorithm that aims to minimize this energy.

Stochastic generative models such as variational autoencoders (VAEs) [24] and generative adversarial networks (GANs) [25] are also used for anomaly detection. Those methods are usually associated with a score function, similar to the reconstruction error used for autoencoder-based models.

An and Cho [26] proposed a VAE-based method for detecting anomalies according to high reconstruction probability. Vasilev et al. [27] applied VAE for anomaly detection of MRI data in the diffusion space (q -space).

Zenati et al. [28] explore GAN-based methods for anomaly detection, that simultaneously learn encoder, generator and discriminator during training. Their procedure reduces the test time since it eliminates the need for recovering a latent representation. A combination of reconstruction and discrimination losses is used to determine whether a sample is anomalous. A similar idea is used in [29], where the score is the “fake-class probability”.

Another idea which directly affects this work is an addition of a linear self-expressive layer to an autoencoder [30]. Such a layer is helpful for extracting useful latent features to tackle unsupervised subspace clustering problems. By imposing the self-expressiveness, the autoencoder is robust to an increasing number of clusters. Although self-expressiveness also improves robustness to noise and out-

liers, [30] aims at clustering and thus its goal is different than ours. Furthermore, their self-expressive energy does not explicitly consider robustness, while ours does. Lezama et al. [31] consider a somewhat parallel idea of imposing a loss function to increase the robustness of representation. However, their goal is to increase the margin between classes and their method only applies to a supervised setting in anomaly detection, where the normal data is multi-modal.

There are many kernel and manifold-learning methods for anomaly detection. Some of them were reviewed in [1]. However, they are not as competitive as the methods reviewed here and are not directly relevant to our work.

1.2. Contribution of this work

This work introduces an RSR layer within an autoencoder. In this way, it enforces an outliers-robust linear structure in the embedding obtained by the encoder. Instead of directly removing outliers according to this enforced structure, which may only be approximate in practice, an outliers-robust energy is used as a regularizer. That is, we suggest minimizing an energy, which is a sum of two components: recovery error obtained by the autoencoder, which expresses the accuracy of the nonlinear dimension reduction, and a robust energy, which is the sum of absolute deviations from the latent subspace (the linear structure mentioned above). We design an architecture which is simple to implement. The RSR layer is not limited to a specific design of RSRAE but can be put into any well-designed autoencoder structure. The combination of an autoencoder with the RSR layer incorporates robustness into the new network.

For the optimization of the total energy we advocate an alternating minimization, though other methods, such as gradient descent applied to the total energy function, are also possible. For the alternating minimization procedure, the epoch time is comparable to other autoencoder structure. Furthermore, our experiments show that RSRAE obtains competitive performance in unsupervised anomaly detection tasks.

Performance guarantees for our method are difficult. We establish instead some preliminary analysis for RSR within GAN. More precisely, we show that a linear WGAN intrinsically incorporates RSR in some special settings, although it is unclear how to impose a linear RSR layer similarly to RSRAE. We further discuss some pure mathematical works that seem relevant to our work and its extensions.

1.3. Structure of the Rest of Paper

The rest of the paper is organized as follows. Section 2 explains the proposed RSRAE by providing details on the RSR layer and the total energy function. Section 3 demonstrates the performance of the proposed method for two artificial datasets. Using these sets, it also validates the choice

$$\mathbf{X} \xrightarrow{\mathcal{E}} \mathbf{Z} \xrightarrow{\mathbf{A}} \tilde{\mathbf{Z}} \xrightarrow{\mathcal{D}} \tilde{\mathbf{X}}$$

Figure 2: The structure of RSRAE.

of norm in the energy function. Section 4 briefly presents and discusses relevant mathematical analysis (proofs are in the appendix). Section 5 illustrates the effectiveness of our method using image data. Section 6 summarizes this work and mentions future directions. The appendix contains proofs of the two propositions stated in this work and complimentary numerical details to the ones stated in the main body of work.

2. RSR layer for outlier removal

The main structure of RSRAE is illustrated in Fig. 2. Here \mathcal{E} denotes an encoder and \mathcal{D} denotes a decoder. Let $\mathbf{X} = \{\mathbf{x}^{(t)}\}_{t=1}^N$ be the input data, which is contained in the Euclidean space \mathbb{R}^M . The latent code $\mathbf{z}^{(t)} = \mathcal{E}(\mathbf{x}^{(t)})$ is a vector in \mathbb{R}^D . The RSR layer is a linear transformation $\mathbf{A} \in \mathbb{R}^{d \times D}$ that reduces the dimensionality to d . That is, $\tilde{\mathbf{z}}^{(t)} = \mathbf{A}\mathbf{z}^{(t)} \in \mathbb{R}^d$. The decoder maps $\tilde{\mathbf{z}}^{(t)}$ to $\tilde{\mathbf{x}}^{(t)}$, which lies in the original ambient space \mathbb{R}^M .

We can write the forward maps in a compact form

$$\mathbf{Z} = \mathcal{E}(\mathbf{X}), \quad \tilde{\mathbf{Z}} = \mathbf{A}\mathbf{Z}, \quad \tilde{\mathbf{X}} = \mathcal{D}(\tilde{\mathbf{Z}}). \quad (1)$$

Ideally, we would like to optimize RSRAE so it only maintains the underlying structure of the normal data. We assume that the original normal data lies on a d -dimensional “manifold” in \mathbb{R}^D and thus the RSR layer embeds its latent code into \mathbb{R}^d . In this ideal optimization setting, the similarity between the input and the output of RSRAE is large whenever the input is normal and small whenever the input is anomalous. Therefore, by thresholding any good similarity measure or the reconstruction error, one may distinguish between normal and anomalous data points.

In practice, the matrix \mathbf{A} and the parameters of \mathcal{E} and \mathcal{D} are obtained by minimizing a loss function, which is a sum of two parts: the reconstruction loss from the autoencoder and the loss from the RSR layer. For $p > 0$, an $\ell_{2,p}$ reconstruction loss for the autoencoder is

$$L_{\text{AE}}^p(\mathcal{E}, \mathbf{A}, \mathcal{D}) = \sum_{t=1}^N \left\| \mathbf{x}^{(t)} - \tilde{\mathbf{x}}^{(t)} \right\|_2^p. \quad (2)$$

In order to motivate our choice of RSR loss, we review a common formulation for the original RSR problem. In this problem one needs to recover a linear subspace, or equivalently an orthogonal projection \mathbf{P} onto this subspace. Assume a dataset $\{\mathbf{y}^{(t)}\}_{t=1}^N$ and let \mathbf{I} denote the identity matrix in the ambient space of the dataset. The goal is to find an orthogonal projector \mathbf{P} of dimension d whose subspace

robustly approximates this dataset. The least q -th power deviations formulation for $q > 0$, or least absolute deviations when $q = 1$, seeks \mathbf{P} that minimizes the loss function [5]

$$\hat{L}(\mathbf{P}) = \sum_{t=1}^N \left\| (\mathbf{I} - \mathbf{P}) \mathbf{y}^{(t)} \right\|_2^q. \quad (3)$$

The solution of this problem is robust to some outliers when $q \leq 1$ [19, 22]; furthermore, $q < 1$ can result in a wealth of local minima and thus $q = 1$ is preferable [19, 22].

A similar loss function to (3) for RSRAE is

$$\begin{aligned} L_{\text{RSR}}^q(\mathbf{A}) &= L_{\text{RSR}_1}(\mathbf{A}) + L_{\text{RSR}_2}(\mathbf{A}) \\ &:= \lambda_1 \sum_{t=1}^N \left\| \mathbf{z}^{(t)} - \mathbf{A}^T \underbrace{\mathbf{A} \mathbf{z}^{(t)}}_{\tilde{\mathbf{z}}^{(t)}} \right\|_2^q + \quad (4) \\ &\quad \lambda_2 \left\| \mathbf{A} \mathbf{A}^T - \mathbf{I}_d \right\|_F, \end{aligned}$$

where \mathbf{A}^T denotes the transpose of \mathbf{A} , \mathbf{I}_d denotes the $d \times d$ identity matrix and $\|\cdot\|_F$ denotes the Frobenius norm. Here $\lambda_1, \lambda_2 > 0$ are predetermined hyperparameters, though we later show that one may solve the underlying problem without using them. We note that the first term in the weighted sum of (4) is close to (3) as long as $\mathbf{A}^T \mathbf{A}$ is close to an orthogonal projector. To enforce this requirement we introduced the second term in the weighted sum of (4). In Section 2.1 we discuss further properties of the RSR energy and its minimization, though this discussion may not generalize to the minimization of the combined energy discussed next.

To emphasize the effect of outlier removal, we take $p = 1$ in (2) and $q = 1$ in (4). That is, we use the $l_{2,1}$ norm, or the formulation of least absolute deviations, for both reconstruction and RSR. The loss function of RSRAE is the sum of the two loss terms in (2) and (4), that is,

$$L_{\text{RSRAE}}(\mathcal{E}, \mathbf{A}, \mathcal{D}) = L_{\text{AE}}^1(\mathcal{E}, \mathbf{A}, \mathcal{D}) + L_{\text{RSR}}^1(\mathbf{A}). \quad (5)$$

Although it is possible to directly minimize L_{RSRAE} with predetermined λ_1 and λ_2 via auto-differentiation, we propose using alternating minimization. This procedure backpropagates the three terms $L_{\text{AE}}^1, L_{\text{RSR}_1}^1, L_{\text{RSR}_2}^1$ and accordingly updates the parameters of RSRAE. It is independent of the values of the parameters λ_1 and λ_2 and we may thus ignore them. Note that the additional gradient step with respect to the RSR loss just updates the parameters in \mathbf{A} . Therefore it does not significantly increase the epoch time of a standard autoencoder for anomaly detection. We summarize our procedure for RSRAE anomaly detection with alternating minimization in Algorithm 1. In doing this we denote the vectors of parameters of the encoder and decoder by $\boldsymbol{\theta}$ and $\boldsymbol{\varphi}$, respectively.

We clarify some guidelines for choosing default parameters, which we follow in all reported experiments. We set

Algorithm 1 RSRAE anomaly detection

Input: Data $\{\mathbf{x}^{(t)}\}_{t=1}^N$; thresholds $\epsilon_{\text{AE}}, \epsilon_{\text{RSR}_1}, \epsilon_{\text{RSR}_2}, \epsilon_{\text{T}}$; architecture & initial parameters of $\mathcal{E}, \mathcal{D}, \mathbf{A}$; # of epochs & batches; learning rate for backpropagation; similarity measure

Output: Labels of data points as normal or anomalous

```

1: for each epoch do
2:   Divide input data into batches
3:   for each batch do
4:     if  $L_{\text{AE}}^1(\boldsymbol{\theta}, \mathbf{A}, \boldsymbol{\varphi}) > \epsilon_{\text{AE}}$  then
5:       Backpropagate  $L_{\text{AE}}^1(\boldsymbol{\theta}, \mathbf{A}, \boldsymbol{\varphi})$  w.r.t.  $\boldsymbol{\theta}, \mathbf{A}, \boldsymbol{\varphi}$  &
       update  $\boldsymbol{\theta}, \mathbf{A}, \boldsymbol{\varphi}$ 
6:     end if
7:     if  $L_{\text{RSR}_1}^1(\mathbf{A}) > \epsilon_{\text{RSR}_1}$  then
8:       Backpropagate  $L_{\text{RSR}_1}^1(\mathbf{A})$  w.r.t.  $\mathbf{A}$  & update  $\mathbf{A}$ 
9:     end if
10:    if  $L_{\text{RSR}_2}^1(\mathbf{A}) > \epsilon_{\text{RSR}_2}$  then
11:      Backpropagate  $L_{\text{RSR}_2}^1(\mathbf{A})$  w.r.t.  $\mathbf{A}$  & update  $\mathbf{A}$ 
12:    end if
13:  end for
14: end for
15: for  $t = 1, \dots, N$  do
16:   Calculate similarity between
    $\mathbf{x}^{(t)}$  and  $\tilde{\mathbf{x}}^{(t)}$ 
17:   if similarity  $\geq \epsilon_{\text{T}}$  then
18:      $\mathbf{x}^{(t)}$  is normal
19:   else
20:      $\mathbf{x}^{(t)}$  is anomalous
21:   end if
22: end for
23: return Normality labels for  $t = 1, \dots, N$ 

```

$\epsilon_{\text{AE}}, \epsilon_{\text{RSR}_1}$ and ϵ_{RSR_2} to be zero. In general, we use networks with dense layers (see Section 3). However, special kinds of data suggest different layers. For example, for image data we use convolutional layers (see Section 5). In general, we prefer to use tanh as the activation function due to its smoothness. However, for data that does not lie in the unit cube, we use a leaky ReLU function. The network parameters and the elements of \mathbf{A} are initialized to i.i.d. standard normal. The learning rate is chosen so that there is a sufficient improvement of the loss values after each epoch. For relatively simple examples (see Section 3) we perform batch gradient descent, that is, we apply one batch that includes the whole data, and set a large number of epochs. On the other hand, for the larger image data of Section 5 we take a small batch size and a smaller number of epochs. Instead of fixing ϵ_{T} , we report Area Under Curve (AUC) and Average Precision (AP) scores for different values of ϵ_{T} . Our default choice for similarity is cosine similarity (see Section 5). However, due to the geometric structure of the artificial data in Section 3, we used negative

squared ℓ_2 distance between $\mathbf{x}^{(t)}$ and $\tilde{\mathbf{x}}^{(t)}$ as “similarity”.

At last, we remark that we executed RSRAE using TensorFlow with few adapted codes written in Keras. We report results of experiments implemented on a Linux machine with 64GB RAM and four GTX1080Ti GPUs.

2.1. Further discussion of the RSR term

In theory, appropriate minimization of only the first term in (4) is sufficient to minimize (4). This result is stated rigorously in Proposition 2.1 and proved in the appendix.

Proposition 2.1. *Assume that $\{\mathbf{z}^{(t)}\}_{t=1}^N \subset \mathbb{R}^D$ spans \mathbb{R}^D , $d \leq D$ and let*

$$\mathbf{A}^* = \underset{\substack{\mathbf{A} \in \mathbb{R}^{d \times D} \\ \text{rank}(\mathbf{A})=d}}{\text{argmin}} \sum_{t=1}^N \left\| \mathbf{z}^{(t)} - \mathbf{A}^T \mathbf{A} \mathbf{z}^{(t)} \right\|_2. \quad (6)$$

Then $\mathbf{A}^* \mathbf{A}^{*T} = \mathbf{I}_d$.

We remark that while the minimization in (6) is intractable, [22] proposes a heuristic to solve it with some weak guarantees and [23] proposes an algorithm with guarantees under some conditions. However, such a minimization is even more difficult when applied to the combined energy in (5), instead of (4). Therefore, we find it necessary to impose the condition that \mathbf{A} is close to a projection.

3. Demonstration of RSRAE for artificial data

We explore the performance of RSRAE and modified versions of it on two artificial datasets of corrupted manifolds. In the first case we observe the difference of RSRAE from a simple least squares autoencoder. In the second case we observe the effect of some changes of the RSRAE loss function, in particular, the removal of the RSR term.

3.1. A corrupted Swiss roll example

We assume corrupted data whose normal part is embedded in a Swiss roll¹, which is a two-dimensional manifold in \mathbb{R}^3 . More precisely, the normal part is obtained by mapping 1,000 points uniformly sampled from the rectangle $[3\pi/2, 9\pi/2] \times [0, 11]$ into \mathbb{R}^3 by the function

$$(s, t) \mapsto (t \cos(t), s, t \sin(t)). \quad (7)$$

The anomalous part is obtained by i.i.d. sampling of 900 points from an isotropic Gaussian distribution in \mathbb{R}^3 with zero mean and standard deviation 2 in any direction. Fig. 3a illustrates such a sample, where the normal part is in green and the anomalous part is in blue.

We construct RSRAE with the following structure. The encoder is composed of fully-connected layers of sizes 3,

32, 64 and 128. The decoder is composed of fully connected layers of sizes 128, 64, 32 and 3. Each fully connected layer is activated by the leaky ReLU function with $\alpha = 0.2$. The intrinsic dimension for the RSR layer is $d = 2$.

For comparison, we construct an autoencoder with the same network structure as the RSRAE but with the mean-square-error (MSE) loss function for reconstruction ($p = 2$ in (2)) and with no RSR loss. Throughout the paper, we refer to such an encoder (with possibly different network structure) by MSEAE. We optimize both models with 10,000 epochs and a batch gradient descent using Adam [32] with a learning rate of 0.01.

The reconstructed data ($\tilde{\mathbf{X}}$) from MSEAE and RSRAE are plotted in Figs. 3b and 3c, respectively. Note that Fig. 3c has a larger axis range from that of Figs. 3a and 3b. Therefore, a truncated version of $\tilde{\mathbf{X}}$ from RSRAE is plotted in Fig. 3d. We note that the set of reconstructed normal points in RSRAE seem to lie on the original manifold, whereas the reconstructed normal points by MSEAE seem to only lie near, but often not on the Swiss roll manifold. More importantly, the anomalous points reconstructed by RSRAE seem to be sufficiently far from the set of original anomalous points, unlike the reconstructed points by MSEAE. Therefore, RSRAE can better distinguish anomalies using the distance between the original and reconstructed points, where small values are obtained for normal points and large ones for anomalous ones.

Figs. 3e and 3f demonstrate this claim. They plot the histograms of the distance between the original and reconstructed points when applying MSEAE and RSRAE, where distances for normal and anomalous points are distinguished by color. Clearly, RSRAE distinguishes normal and anomalous data better than MSEAE.

3.2. An example of two intersecting curves

We consider data points that lie on two intersecting curves in \mathbb{R}^2 , where one curve is “more significant”, that is, it contains more points than the other. The points on the more significant curve are normal and the points on the less significant curve are anomalous. We generate the curves as follows. We randomly form two orthogonal lines in \mathbb{R}^2 . We independently sample 1,000 normal points from a standard normal distribution on the first line. We consider the following possible number of anomalous points: 100, 300, 500, 700 and 900. For any fixed number, we independently sample this number of points from a standard normal distribution on the second line. To make the setting nonlinear, we transform each data point (s, t) to $(\sin(s), \sin(t))$. As a result, we get data points that lie on two intersecting curves in \mathbb{R}^2 . An example with 100 anomalous points is illustrated in Fig. 4.

We examine here the effect of various modifications of the energy on the reconstruction by RSRAE. In particular,

¹https://scikit-learn.org/stable/modules/generated/sklearn.datasets.make_swiss_roll.html

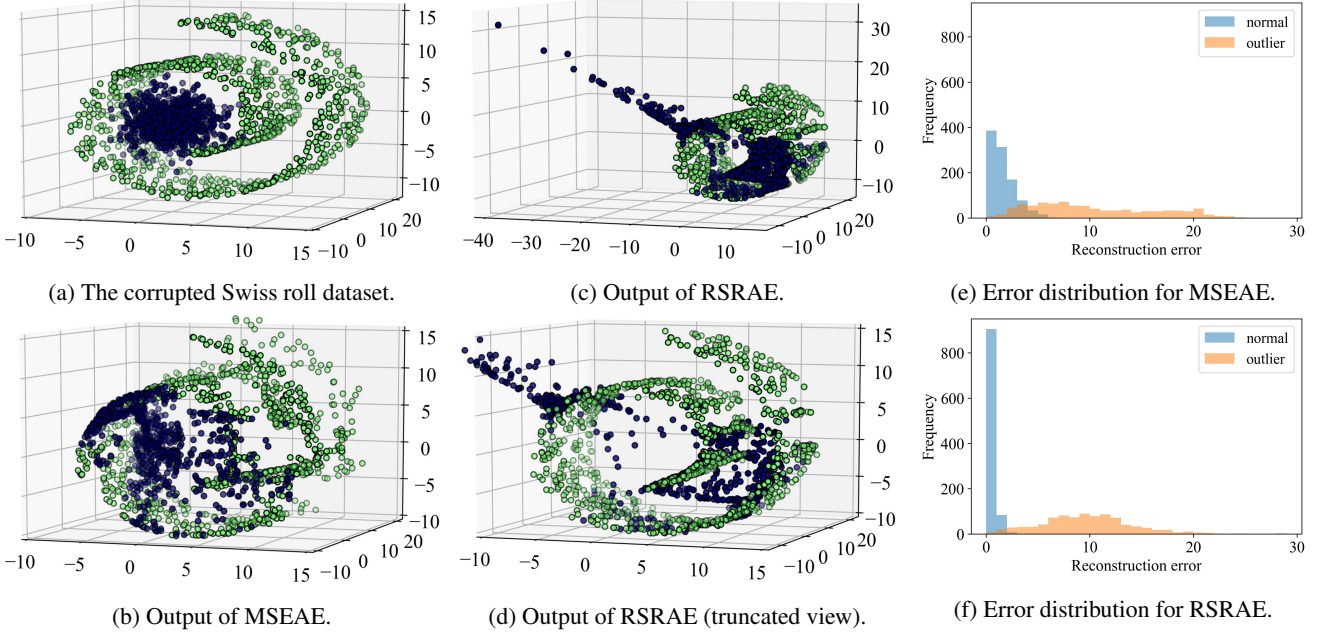


Figure 3: Demonstration of the corrupted Swiss roll dataset and performance by MSEAE and RSRAE.

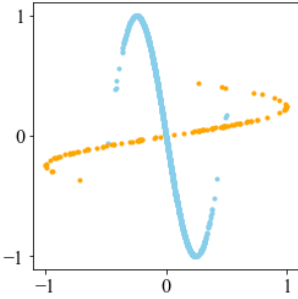


Figure 4: Illustration of a dataset generated along two intersecting curves, where one curve is more significant. There are 1,000 blue points on the more significant curve and 100 orange points on the other curve.

we try to address the natural question of whether the use of the loss function in (2) with $p = 1$, or even $p = 2$, is sufficient for good recovery or whether the addition of the RSR loss in (2) significantly improves the recovery. We also examine the difference between an alternating implementation vs. auto-differentiation of the combined energy.

We train RSRAE with the following structure. The encoder is composed of fully-connected layers of sizes 3, 32 and 32, and the decoder is composed of fully-connected layers of sizes 32, 32 and 3. Each fully-connected layer in RSRAE is activated by the tanh function. The RSR loss assumes the intrinsic dimension $d = 1$.

We consider the following loss functions for fitting the

autoencoder:

- L_{AE}^2 : the MSEAE loss;
- L_{AE}^1 : the $\ell_{2,1}$ reconstruction loss;
- $L_{AE}^1 + L_{RSR}^1$: the RSRAE loss with direct auto-differentiation, where $\lambda_1 = \lambda_2 = 0.5$;
- L_{AE}^1 & L_{RSR}^1 : the RSRAE loss optimized by alternating minimization.

We optimize each loss function 10 times with random initialization of the network parameters. The learning rate is 0.001, the number of epochs is 500 and batch gradient descent is applied. We compute both the AUC and AP scores and report them in Fig. 5 (precise scores also appear in the appendix). We first note that when using L_{AE}^1 or L_{AE}^2 and the outlier ratio is not small, both the AUC score and AP score are very low. While reconstruction with L_{AE}^1 is better than with L_{AE}^2 , it is still not comparable with reconstruction involving an RSR layer. Second of all, the alternating minimization (L_{AE}^1 & L_{AE}^2) always performs better than $L_{AE}^1 + L_{AE}^2$. In particular, for a small portion of outliers, $L_{AE}^1 + L_{RSR}^1$ does not perform well.

4. Related theory for RSR penalty

Section 3 demonstrated the effectiveness of the RSR layer in removing outliers in artificial cases. The idea of an RSR layer may impose robustness for many other unsupervised learning frameworks which incorporate nonlinear dimension reduction. While it is extremely difficult to guarantee the performance of the resulting anomaly detection even for simple cases, it is very important to establish re-

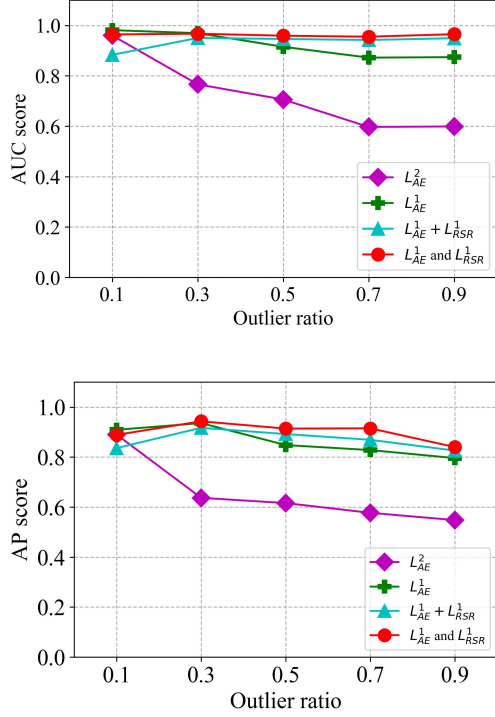


Figure 5: AUC and AP scores for two intersecting curves.

lated theoretical understanding.

First, we show that Wasserstein-GAN (WGAN) [33, 34] has an energy function (the 1-Wasserstein distance) which intrinsically relates to the RSR loss. We find this relationship interesting and relevant to anomaly detection via neural networks.

Let W_p denote the p -Wasserstein distance in \mathbb{R}^D for some $p \geq 1$. That is, for two distributions μ, ν in \mathbb{R}^D ,

$$W_p(\mu, \nu) = \left(\inf_{\pi \in \Pi(\mu, \nu)} \mathbb{E}_{(\mathbf{x}, \mathbf{y}) \sim \pi} \|\mathbf{x} - \mathbf{y}\|_2^p \right)^{1/p}, \quad (8)$$

where $\Pi(\mu, \nu)$ is the set of joint distributions with μ, ν as marginals. The following proposition (proved in the appendix) implies that minimizing W_p for Gaussians is closely related to minimizing the loss function (3).

Proposition 4.1. *Let $p \geq 1$ and $\mu \sim \mathcal{N}(\mathbf{m}_X, \Sigma_X)$, where $\mathbf{m}_X \in \mathbb{R}^D$ and Σ_X is the covariance matrix that has full rank D . Then*

$$\begin{aligned} \min_{\nu \sim \mathcal{N}(\mathbf{m}_Y, \Sigma_Y)} \quad & W_p(\mu, \nu) \\ \text{s.t.} \quad & \mathbf{m}_Y \in \mathbb{R}^D \\ & \text{rank}(\Sigma_Y) = d \end{aligned} \quad (9)$$

is achieved when $\nu \sim \mathcal{N}(\mathbf{m}_X, \mathbf{P}_{\mathcal{L}} \Sigma_X \mathbf{P}_{\mathcal{L}})$, where

$$\mathcal{L} = \underset{\dim \mathcal{L} = d}{\operatorname{argmin}} \mathbb{E} \|X - \mathbf{P}_{\mathcal{L}} X\|_2^p. \quad (10)$$

Note that a WGAN is trained to minimize the W_1 distance between the target data distribution and the generated distribution. Note also that the objective function in (10) is essentially (3). Therefore, the above proposition with $p = 1$ implies that if the target data is drawn from a Gaussian distribution in the ambient space and if WGAN has a linear generator whose input is a d -dimensional Gaussian, then WGAN learns the d -dimensional RSR subspace of the target data.

Unfortunately, when the generator of the WGAN is non-linear, the behavior of WGAN is intractable. Furthermore, it is unclear how to incorporate an RSR layer within WGAN or GAN. At last, training a WGAN is not exactly the same as minimizing the W_1 distance [34], since it is difficult to impose the Lipschitz constraint for a neural network. Indeed, in general, GAN-based anomaly detection is not competitive (see e.g. the results from GAN models in [35] and in [28]). A proper design of GAN-based anomaly detection is left for future work.

Next, we review some pure mathematical work that we find relevant to this discussion. We note that a complex network can represent a large class of functions. Consequently, for a sufficiently complex network, minimizing the loss function in (2) results in minimum value zero. In this case the minimizing “manifold” contains the original data, including the outliers. On the other hand, the RSR loss term imposes fitting a subspace that robustly fits only part of the data and thus cannot result in minimum value zero. Nevertheless, imposing a subspace constraint might be too restrictive, even in the latent space. A seminal work by Peter Jones [36] studies optimal types of curves that contain general sets. This work relates the construction and optimal properties of these curves with multiscale approximation of the underlying set by lines. It was generalized to higher dimensions in [37] and to a setting relevant to outliers in [38]. These works suggest loss functions that incorporate several linear RSR layers from different scales. Nevertheless, their pure setting does not directly apply to our setting. We leave further theoretical developments and implementation for future work.

5. Numerical experiments with image data

We test our method on two image datasets: MNIST [39] and Fashion-MNIST [40]. Both are composed of 28×28 grayscale images, which are categorized according to 10 classes. There are 60,000 training images and 10,000 test images. We only use the set of test images. In each experiment we fix a class with label $I \in \{0, 1, \dots, 9\}$ and let the normal images be all the test images in class I (there are around 1000 test images in each class). We fix $c \in \{0.1, 0.3, 0.5, 0.7, 0.9\}$ and randomly sample $c \times 1,000$ images from the rest of classes. Therefore the fraction of outliers is approximately c .

In Section 5.1 we review the benchmarks used for comparison and the experimental setting. In Section 5.2 we report and discuss the numerical results.

5.1. Benchmarks and setting

We compare RSRAE with the following benchmarks.

ℓ_2 **Normalized Autoencoder (NAE)** [11]: NAE is similar to MSEAE, but it also imposes ℓ_2 normalization of the latent code. It achieved state-of-the-art results for unsupervised anomaly detection with multi-modal normal data. We run NAE with a single class and thus omit its k -means step.

Deep Autoencoding Gaussian Mixture Model (DAGMM) [12]: DAGMM is a deep autoencoder model. It optimizes an end-to-end structure that contains both an autoencoder and an estimator for Gaussian Mixture Model. It achieved state-of-the-art results on unsupervised anomaly detection for network attack data.

Deep Structured Energy-Based Models (DSEBMs) [13]: The energy function of DSEBMs is outputted by a deep neural network. It is used as negative similarity instead of the reconstruction error. DSEBMs achieved state-of-the-art results for unsupervised anomaly detection with image data.

Geometric Transformations (GeoTrans) [35]: GeoTrans applies dozens of geometric transforms to the given images and consequently creates a self-labeled dataset, where the labels are the types of transformations. Its anomaly detection is based on Dirichlet Normality score according to the softmax output from a classification network for the labels. It is a relatively new and effective method.

We adapt the network structures of DSEBMs, DAGMM and GeoTrans from [35]² and slightly modified their codes to adapt to our data and machine. Since there is no available code for NAE, we implemented it on our own, where we adapted the autoencoder structure of Deep Convolutional Embedded Clustering (DCEC) [41]³ by adding ℓ_2 normalization. For both NAE and RSRAE, we use the cosine similarity.

For RSRAE, we adapt the convolutional layers from DCEC [41] but impose the activation function to be tanh. Also, batch normalization is applied for each convolutional layer to be consistent with the other methods. The intrinsic dimension for RSR is chosen to be 10 since it is approximately the intrinsic dimension of the MNIST data [42]. Additional details appear in the appendix.

For each experiment, the RSRAE model is optimized with Adam using a learning rate of 0.00025 and 200 epochs. The batch size is 128 for each gradient step.

5.2. Results

We summarize the precision and recall of our experiments by the AP and AUC scores. We remark that we did not record precision-recall-F1 scores [11, 12] since it requires a choice of threshold, which is unclear in practical scenarios when the outlier ratio is unknown.

We average these scores over 10 runs with different random initialization. For brevity of presentation, we also average the scores among all classes.

Fig. 6 presents the averaged results for MNIST (detailed tables for each class and outlier ratio are reported in the appendix). On average, RSRAE consistently outperforms the other methods. We remark though that for the digits 4 and 5 GeoTrans often performs better than RSRAE and for the digit 1 NAE sometimes performs better than RSRAE. DAGMM does not perform well and it may be too difficult to train the estimation network for image data (it was tested before on network attack data).

For Fashion-MNIST, we average the results, while excluding the class “sandals” and present them in Fig. 7 (complete tables are in the appendix). We exclude “sandals” for two reasons. First of all, the images of “sandals” look anomalous as they are too sparse. Second of all, the AUC score for RSRAE is extremely small and this is not the case for other classes. This suggests that RSRAE treats “sandals” as outliers. For all the other classes, RSRAE shows very competitive performance. The only other method which has a similar performance as RSRAE, when excluding “sandals”, is DSEBMs, but RSRAE performs better with large ratios of outliers. If “sandals” is included, then overall DSEBMs performs better.

6. Conclusion and future work

We construct a simple but effective RSR layer within the autoencoder structure for anomaly detection. It is easy to use and adapt. We have demonstrated competitive results for image data and believe that it can be useful in many other computer vision applications.

There are several directions for further exploration of the RSR loss in unsupervised deep learning models for anomaly detection. First, we are interested in theoretical guarantees for RSRAE. A more direct subproblem is understanding the geometric structure of the “manifold” learned by RSRAE. Second, as mentioned earlier, [36, 37, 38] suggest the use of several RSR layers in a multiscale fashion. It is interesting to explore this direction and its theoretical justification. Third, one may try to incorporate an RSR layer in other neural networks for anomaly detection that use nonlinear dimension reduction. We hope that some of these methods may be easier to directly analyze than our proposed method. At last, we are curious about successful incorporation of robust metrics for more complex models such as GANs. In

²<https://github.com/izikgo/AnomalyDetectionTransformations>

³<https://github.com/XifengGuo/DCEC>

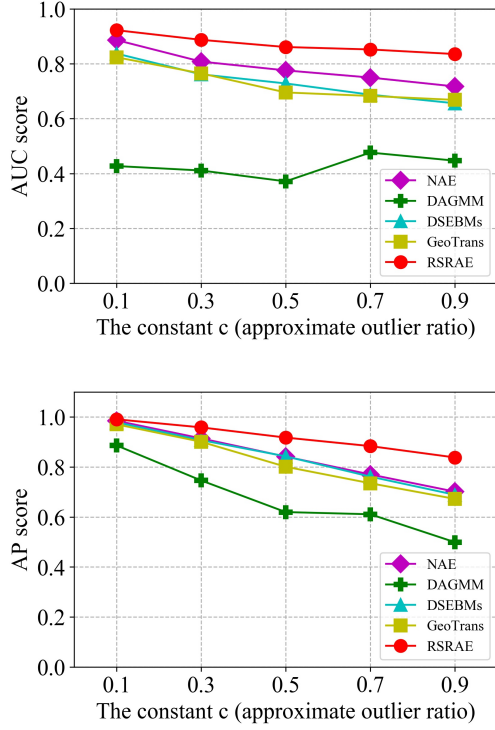


Figure 6: The AUC and AP scores for MNIST.

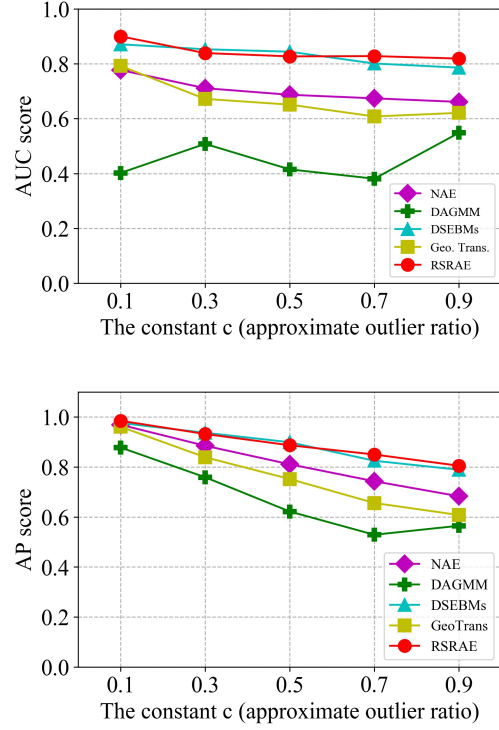


Figure 7: The AUC and AP scores for Fashion-MNIST excluding “sandals”.

particular, we wonder about extensions of the theory established here for WGAN when considering a more general setting.

Acknowledgement

This research has been supported by NSF award DMS-18-30418. We thank Teng Zhang for his help with proving Proposition 4.1 (we discussed a related but different proposition with similar ideas of proofs). We thank Madeline Handschy for commenting on an earlier version of this paper.

References

- [1] V. Chandola, A. Banerjee, and V. Kumar, “Anomaly detection: A survey,” *ACM computing surveys (CSUR)*, vol. 41, no. 3, p. 15, 2009.
- [2] Y. Xia, X. Cao, F. Wen, G. Hua, and J. Sun, “Learning discriminative reconstructions for unsupervised outlier removal,” in *Proceedings of the IEEE International Conference on Computer Vision*, pp. 1511–1519, 2015.
- [3] W. Liu, W. Luo, D. Lian, and S. Gao, “Future frame prediction for anomaly detection—a new baseline,” in *Proceedings of the IEEE Conference on Computer Vision and Pattern Recognition*, pp. 6536–6545, 2018.
- [4] M.-L. Shyu, S.-C. Chen, K. Sarinapakorn, and L. Chang, “A novel anomaly detection scheme based on principal component classifier,” in *Proc. ICDM Foundation and New Direction of Data Mining workshop*, 2003, pp. 172–179, 2003.
- [5] G. Lerman and T. Maunu, “An overview of robust subspace recovery,” *Proceedings of the IEEE*, vol. 106, no. 8, pp. 1380–1410, 2018.
- [6] N. Vaswani and P. Narayanamurthy, “Static and dynamic robust PCA and matrix completion: A review,” *Proceedings of the IEEE*, vol. 106, no. 8, pp. 1359–1379, 2018.
- [7] J. Wright, A. Ganesh, S. Rao, Y. Peng, and Y. Ma, “Robust principal component analysis: Exact recovery of corrupted low-rank matrices via convex optimization,” in *Advances in neural information processing systems*, pp. 2080–2088, 2009.
- [8] C. Zhou and R. C. Paffenroth, “Anomaly detection with robust deep autoencoders,” in *Proceedings of the 23rd ACM SIGKDD International Conference on Knowledge Discovery and Data Mining*, pp. 665–674, ACM, 2017.
- [9] R. Paffenroth, K. Kay, and L. Servi, “Robust PCA for anomaly detection in cyber networks,” *arXiv preprint arXiv:1801.01571*, 2018.
- [10] F. De La Torre and M. J. Black, “A framework for robust subspace learning,” *International Journal of Computer Vision*, vol. 54, no. 1-3, pp. 117–142, 2003.
- [11] C. Aytekin, X. Ni, F. Cricri, and E. Aksu, “Clustering and unsupervised anomaly detection with l_2 normalized deep auto-

- encoder representations,” in *2018 International Joint Conference on Neural Networks (IJCNN)*, pp. 1–6, July 2018.
- [12] B. Zong, Q. Song, M. R. Min, W. Cheng, C. Lumezanu, D. Cho, and H. Chen, “Deep autoencoding gaussian mixture model for unsupervised anomaly detection,” in *International Conference on Learning Representations*, 2018.
- [13] S. Zhai, Y. Cheng, W. Lu, and Z. Zhang, “Deep structured energy based models for anomaly detection,” *arXiv preprint arXiv:1605.07717*, 2016.
- [14] G. A. Watson, *Some Problems in Orthogonal Distance and Non-Orthogonal Distance Regression*. Defense Technical Information Center, 2001.
- [15] C. Ding, D. Zhou, X. He, and H. Zha, “R1-PCA: rotational invariant l_1 -norm principal component analysis for robust subspace factorization,” in *Proceedings of the 23rd international conference on Machine learning*, pp. 281–288, ACM, 2006.
- [16] T. Zhang, A. Szlam, and G. Lerman, “Median K-flats for hybrid linear modeling with many outliers,” in *Computer Vision Workshops (ICCV Workshops), 2009 IEEE 12th International Conference on*, pp. 234–241, IEEE, 2009.
- [17] M. McCoy and J. A. Tropp, “Two proposals for robust PCA using semidefinite programming,” *Electronic Journal of Statistics*, vol. 5, pp. 1123–1160, 2011.
- [18] H. Xu, C. Caramanis, and S. Sanghavi, “Robust PCA via outlier pursuit,” *IEEE Trans. Information Theory*, vol. 58, no. 5, pp. 3047–3064, 2012.
- [19] G. Lerman and T. Zhang, “ l_p -recovery of the most significant subspace among multiple subspaces with outliers,” *Constructive Approximation*, vol. 40, no. 3, pp. 329–385, 2014.
- [20] T. Zhang and G. Lerman, “A novel M-estimator for robust PCA,” *Journal of Machine Learning Research*, vol. 15, no. 1, pp. 749–808, 2014.
- [21] G. Lerman, M. B. McCoy, J. A. Tropp, and T. Zhang, “Robust computation of linear models by convex relaxation,” *Foundations of Computational Mathematics*, vol. 15, no. 2, pp. 363–410, 2015.
- [22] G. Lerman and T. Maunu, “Fast, robust and non-convex subspace recovery,” *Information and Inference: A Journal of the IMA*, vol. 7, no. 2, pp. 277–336, 2017.
- [23] T. Maunu, T. Zhang, and G. Lerman, “A well-tempered landscape for non-convex robust subspace recovery,” *arXiv preprint arXiv:1706.03896*, 2017.
- [24] D. P. Kingma and M. Welling, “Auto-encoding variational Bayes,” *arXiv preprint arXiv:1312.6114*, 2013.
- [25] I. Goodfellow, J. Pouget-Abadie, M. Mirza, B. Xu, D. Warde-Farley, S. Ozair, A. Courville, and Y. Bengio, “Generative adversarial nets,” in *Advances in neural information processing systems*, pp. 2672–2680, 2014.
- [26] J. An and S. Cho, “Variational autoencoder based anomaly detection using reconstruction probability,” *Speial Lecture on IE*, vol. 2, pp. 1–18, 2015.
- [27] A. Vasilev, V. Golkov, I. Lipp, E. Sgarlata, V. Tomassini, D. K. Jones, and D. Cremers, “q-space novelty detection with variational autoencoders,” *arXiv preprint arXiv:1806.02997*, 2018.
- [28] H. Zenati, C. S. Foo, B. Lecouat, G. Manek, and V. R. Chandrasekhar, “Efficient GAN-based anomaly detection,” 2018.
- [29] M. Kliger and S. Fleishman, “Novelty detection with GAN,” 2018.
- [30] P. Ji, T. Zhang, H. Li, M. Salzmann, and I. Reid, “Deep subspace clustering networks,” in *Advances in Neural Information Processing Systems*, pp. 24–33, 2017.
- [31] J. Lezama, Q. Qiu, P. Musé, and G. Sapiro, “OLÉ: Orthogonal low-rank embedding—a plug and play geometric loss for deep learning,” in *Proceedings of the IEEE Conference on Computer Vision and Pattern Recognition*, pp. 8109–8118, 2018.
- [32] D. P. Kingma and J. Ba, “Adam: A method for stochastic optimization,” *arXiv preprint arXiv:1412.6980*, 2014.
- [33] M. Arjovsky, S. Chintala, and L. Bottou, “Wasserstein GAN,” *arXiv preprint arXiv:1701.07875*, 2017.
- [34] I. Gulrajani, F. Ahmed, M. Arjovsky, V. Dumoulin, and A. C. Courville, “Improved training of Wasserstein GANs,” in *Advances in Neural Information Processing Systems*, pp. 5767–5777, 2017.
- [35] I. Golan and R. El-Yaniv, “Deep anomaly detection using geometric transformations,” in *Advances in Neural Information Processing Systems*, pp. 9781–9791, 2018.
- [36] P. Jones, “Rectifiable sets and the traveling salesman problem,” *Invent Math*, vol. 102, no. 1, pp. 1–15, 1990.
- [37] G. David and S. Semmes, *Analysis of and on uniformly rectifiable sets*, vol. 38 of *Mathematical surveys and monographs*. Providence, RI: American Mathematical Society, 1993.
- [38] G. Lerman, “Quantifying curvelike structures of measures by using L_2 Jones quantities,” *Comm. Pure Appl. Math.*, vol. 56, no. 9, pp. 1294–1365, 2003.
- [39] Y. LeCun, C. Cortes, and C. Burges, “MNIST handwritten digit database,” *AT&T Labs [Online]*. Available: <http://yann.lecun.com/exdb/mnist>, vol. 2, p. 18, 2010.
- [40] H. Xiao, K. Rasul, and R. Vollgraf, “Fashion-MNIST: a novel image dataset for benchmarking machine learning algorithms,” *arXiv preprint arXiv:1708.07747*, 2017.
- [41] X. Guo, X. Liu, E. Zhu, and J. Yin, “Deep clustering with convolutional autoencoders,” *International Conference on Neural Information Processing, ICONIP 2017: Neural Information Processing*, vol. LNCS, 10635, pp. 373–382, 2017.
- [42] E. Facco, M. d’Errico, A. Rodriguez, and A. Laio, “Estimating the intrinsic dimension of datasets by a minimal neighborhood information,” *Scientific reports*, vol. 7, no. 1, p. 12140, 2017.

A. Supplemental details

A.1. Proof of Proposition 2.1

Let \mathbf{A}^* be an optimizer of (6) and \mathbf{P}^* denote the orthogonal projection onto the range of $\mathbf{A}^{*\top}\mathbf{A}^*$. Note that \mathbf{P}^* can be written as $\tilde{\mathbf{A}}^\top\tilde{\mathbf{A}}$, where $\tilde{\mathbf{A}}$ is a $d \times D$ matrix composed of an orthonormal basis of the range of \mathbf{P}^* . Therefore, being an optimum of (6), \mathbf{A}^* satisfies

$$\left\| \mathbf{z}^{(t)} - \mathbf{P}^* \mathbf{z}^{(t)} \right\|_2 \geq \left\| \mathbf{z}^{(t)} - \mathbf{A}^{*\top} \mathbf{A}^* \mathbf{z}^{(t)} \right\|_2, \quad t = 1, \dots, N. \quad (11)$$

On the other hand, the definition of orthogonal projection implies that

$$\left\| \mathbf{z}^{(t)} - \mathbf{P}^* \mathbf{z}^{(t)} \right\|_2 \leq \left\| \mathbf{z}^{(t)} - \mathbf{A}^{*\top} \mathbf{A}^* \mathbf{z}^{(t)} \right\|_2, \quad t = 1, \dots, N. \quad (12)$$

That is, equality is obtained in (11) and (12). This equality and the fact that \mathbf{P}^* is a projection on the range of $\mathbf{A}^{*\top}\mathbf{A}^*$ imply that

$$\mathbf{P}^* \mathbf{z}^{(t)} = \mathbf{A}^{*\top} \mathbf{A}^* \mathbf{z}^{(t)}, \quad t = 1, \dots, N. \quad (13)$$

Since $\{\mathbf{z}^{(t)}\}_{t=1}^N$ spans \mathbb{R}^D , (13) results in

$$\mathbf{P}^* = \mathbf{A}^{*\top} \mathbf{A}^*, \quad (14)$$

which further implies that

$$\mathbf{A}^* \mathbf{A}^{*\top} \mathbf{A}^* = \mathbf{A}^* \mathbf{P}^* = \mathbf{A}^*. \quad (15)$$

Combining this observation ($\mathbf{A}^* \mathbf{A}^{*\top} \mathbf{A}^* = \mathbf{A}^*$) with the constraint that \mathbf{A}^* has a full rank, we conclude that $\mathbf{A}^* \mathbf{A}^{*\top} = \mathbf{I}_d$.

A.2. Detailed results for the intersected curves in Section 3.2

Table 1 reports the numerical results for the example of intersecting curves described in Section 3.2. The constant c in this table represents the outlier ratio.

c	L_{AE}^2		L_{AE}^1		$L_{\text{AE}}^1 + L_{\text{RSR}}^1$		$L_{\text{AE}}^1 \& L_{\text{RSR}}^1$	
	AUC	AP	AUC	AP	AUC	AP	AUC	AP
0.1	0.960	0.890	0.981	0.909	0.883	0.836	0.964	0.889
0.3	0.766	0.637	0.969	0.936	0.950	0.917	0.967	0.943
0.5	0.706	0.616	0.915	0.848	0.946	0.892	0.959	0.914
0.7	0.597	0.577	0.872	0.828	0.942	0.869	0.955	0.915
0.9	0.599	0.548	0.874	0.796	0.949	0.826	0.965	0.840

Table 1: Averaged AUC and AP scores for the example of intersecting cures. The averages are taken over 10 runs. The dataset is the same for all 10 runs, but the network parameters are randomly initialized for each run.

A.3. Proof of Proposition 4.1

We denote the subspace \mathcal{L} in the left hand side of (10) by \mathcal{L}^* in order to distinguish it from the generic notation \mathcal{L} for subspaces. We arbitrarily fix a random variable $X \sim \mathcal{N}(\mathbf{m}_X, \Sigma_X)$, that is, X has density μ . We also arbitrarily fix $\pi \in \Pi(\mu, \nu)$. We note that

$$\begin{aligned} & \mathbb{E}_{(X,Y) \sim \pi} \|X - Y\|_2^p \\ &= \int_{\mathbb{R}^D} \int_{\mathbb{R}^D} \|\mathbf{x} - \mathbf{y}\|_2^p \pi(\mathbf{x}, \mathbf{y}) d\mathbf{x} d\mathbf{y} \\ &\geq \min_{\dim \mathcal{L} = d} \int_{\mathbb{R}^D} \text{dist}(\mathbf{x}, \mathcal{L})^p \int_{\mathbb{R}^D} \pi(\mathbf{x}, \mathbf{y}) d\mathbf{y} d\mathbf{x} \\ &= \min_{\dim \mathcal{L} = d} \int_{\mathbb{R}^D} \text{dist}(\mathbf{x}, \mathcal{L})^p \mu(\mathbf{x}) d\mathbf{x} \\ &= \min_{\dim \mathcal{L} = d} \mathbb{E} \|X - \mathbf{P}_{\mathcal{L}} X\|_2^p. \end{aligned} \quad (16)$$

The inequality in (16) holds since X is fixed and Y satisfies $(X, Y) \sim \pi$, so the distribution of Y is $\mathcal{N}(\mathbf{m}_Y, \Sigma_Y)$. Therefore, almost surely, Y takes values in the d -dimensional affine subspace $\{\mathbf{y} \in \mathbb{R}^D : \mathbf{y} - \mathbf{m}_Y \in \text{range}(\Sigma_Y)\}$. Furthermore, we note that equality in (16) is achieved when $Y = \mathbf{P}_{\mathcal{L}^*} X$.

We conclude the proof by showing that

$$\mathbf{m}_X \in \mathcal{L}^*. \quad (17)$$

Indeed, (17) implies that the orthogonal projection of $X \sim \mathcal{N}(\mathbf{m}_X, \Sigma_X)$ onto \mathcal{L}^* results in a random variable with distribution $\nu \sim \mathcal{N}(\mathbf{m}_X, \mathbf{P}_{\mathcal{L}^*} \Sigma_X \mathbf{P}_{\mathcal{L}^*})$. By the above observation about the optimality of $Y = \mathbf{P}_{\mathcal{L}^*} X$, the density of this distribution is the optimal solution of (9).

To prove (17), we assume without loss of generality that $\mathbf{m}_X = \mathbf{0}$. Denote the orthogonal projection of the origin onto the affine subspace \mathcal{L}^* by $\mathbf{m}_{\mathcal{L}^*}$ and let $\mathcal{L}_0 = \mathcal{L}^* - \mathbf{m}_{\mathcal{L}^*}$. We need to show that $\mathcal{L}^* = \mathcal{L}_0$, or equivalently, $\mathbf{m}_{\mathcal{L}^*} = \mathbf{0}$. We note \mathcal{L}_0 is a linear subspace, $\mathbf{m}_{\mathcal{L}^*}$ is orthogonal to \mathcal{L}_0 and thus there exists a rotation matrix \mathbf{O} such that

$$\mathbf{O}\mathcal{L}_0 = \{(0, \dots, 0, z_{D-d+1}, \dots, z_D) : z_{D-d+1}, \dots, z_D \in \mathbb{R}\}, \quad (18)$$

and

$$\mathbf{O}\mathbf{m}_{\mathcal{L}^*} = (m_1, \dots, m_{D-d}, 0, \dots, 0). \quad (19)$$

For any $\mathbf{x} \in \mathbb{R}^D$ we note that $\mu(\mathbf{x}) = \mu(-\mathbf{x})$ since μ is Gaussian. Using this observation, other basic observations and the notation $\mathbf{O}\mathbf{x} = (x'_1, \dots, x'_D)$ we obtain that

$$\begin{aligned} & \text{dist}(\mathbf{x}, \mathcal{L}^*)^p \mu(\mathbf{x}) + \text{dist}(-\mathbf{x}, \mathcal{L}^*)^p \mu(-\mathbf{x}) \\ &= (\text{dist}(\mathbf{x}, \mathcal{L}^*)^p + \text{dist}(-\mathbf{x}, \mathcal{L}^*)^p) \mu(\mathbf{x}) \\ &= (\text{dist}(\mathbf{O}\mathbf{x}, \mathbf{O}\mathcal{L}^*)^p + \text{dist}(-\mathbf{O}\mathbf{x}, \mathbf{O}\mathcal{L}^*)^p) \mu(\mathbf{x}) \\ &= \left(\left(\sum_{i=1}^{D-d} (x'_i - m_i)^2 \right)^{p/2} + \left(\sum_{i=1}^{D-d} (-x'_i - m_i)^2 \right)^{p/2} \right) \mu(\mathbf{x}) \\ &= \left(\left(\sum_{i=1}^{D-d} (x'_i - m_i)^2 \right)^{p/2} + \left(\sum_{i=1}^{D-d} (x'_i + m_i)^2 \right)^{p/2} \right) \mu(\mathbf{x}) \\ &\geq 2 \left(\sum_{i=1}^{D-d} x_i'^2 \right)^{p/2} \mu(\mathbf{x}) \\ &= 2 \text{dist}(\mathbf{O}\mathbf{x}, \mathbf{O}\mathcal{L}_0)^p \mu(\mathbf{x}) \\ &= 2 \text{dist}(\mathbf{x}, \mathcal{L}_0)^p \mu(\mathbf{x}) \\ &= (\text{dist}(\mathbf{x}, \mathcal{L}_0)^p + \text{dist}(-\mathbf{x}, \mathcal{L}_0)^p) \mu(\mathbf{x}) \\ &= \text{dist}(\mathbf{x}, \mathcal{L}_0)^p \mu(\mathbf{x}) + \text{dist}(-\mathbf{x}, \mathcal{L}_0)^p \mu(-\mathbf{x}). \end{aligned} \quad (20)$$

The inequality in (20) follows from the fact that for $p \geq 1$, the function $\|\cdot\|_2^p$ is convex as it is a composition of the convex function $\|\cdot\|_2 : \mathbb{R}^d \rightarrow \mathbb{R}_+$ and the increasing convex function $(\cdot)^p : \mathbb{R}_+ \rightarrow \mathbb{R}_+$. Equality is achieved in (20) if $m_i = 0$ for $i = 1, \dots, D-d$, that is, $\mathcal{L}^* = \mathcal{L}_0$.

Integrating the left and right hand sides of (20) over \mathbb{R}^D results in

$$\int_{\mathbb{R}^D} \text{dist}(\mathbf{x}, \mathcal{L}^*)^p \mu(\mathbf{x}) d\mathbf{x} \geq \int_{\mathbb{R}^D} \text{dist}(\mathbf{x}, \mathcal{L}_0)^p \mu(\mathbf{x}) d\mathbf{x}. \quad (21)$$

Since \mathcal{L}^* is a minimizer among all affine subspaces of rank d of $\int_{\mathbb{R}^D} \text{dist}(\mathbf{x}, \mathcal{L})^p \mu(\mathbf{x}) d\mathbf{x} = \mathbb{E} \|\mathbf{X} - \mathbf{P}_{\mathcal{L}} \mathbf{X}\|_2^p$, equality is obtained in (21). Consequently, equality is obtained, almost everywhere, in (20). Therefore, $\mathcal{L}^* = \mathcal{L}_0$ and the claim is proved.

We remark that the above proposition holds for any $p \geq 1$. However, the only interesting case is $p = 1$, since there is no p -Wasserstein GAN for $p \neq 1$. For the case $p = 1$, the above proposition implies intrinsic relation between the RSR energy and WGAN when the generator of the WGAN is linear. If, however, the generator of a WGAN is nonlinear, its output is not necessarily Gaussian, no matter if the noise is Gaussian. It will be interesting to impose a “linear condition” similar to the RSR layer. However, it is unclear to us how to do this.

A.4. RSRAE structure used in Section 5

For RSRAE, the encoder consists of three convolutional layers:

- Conv1: 5×5 kernels with 32 output channels, strides 2, and zero padding; followed by batch normalization and tanh;
- Conv2: 5×5 kernels with 64 output channels, strides 2, and zero padding; followed by batch normalization and tanh;
- Conv3: 3×3 kernels with 128 output channels, strides 2, and no padding; followed by batch normalization and tanh.

The output of the encoder is flattened as a vector of dimension 1,152. For the RSR layer, $\mathbf{A} \in \mathbb{R}^{10 \times 1,152}$.

For the decoder, first there is a dense layer that maps the output of the RSR layer into a vector of dimension 1,152, which is reshaped into a tensor of dimension $3 \times 3 \times 128$, activated by tanh. It is then followed by three deconvolutional layers:

- Deconv1: 3×3 kernels with 64 output channels, strides 2, and no padding; followed by batch normalization and tanh;
- Deconv2: 5×5 kernels with 32 output channels, strides 2, and zero padding; followed by batch normalization and tanh;
- Deconv3: 5×5 kernels with 1 output channel, strides 2, and zero padding; followed by tanh.

A.5. Detailed results for MNIST in Section 5

The following tables report the AUC and AP scores of RSRAE and different benchmarks for MNIST. Each table reports the results for a specific constant c , where c represents the approximate outlier ratio.

Normal class	NAE		DAGMM		DSEBMs		GeoTrans		RSRAE	
	AUC	AP	AUC	AP	AUC	AP	AUC	AP	AUC	AP
0	0.952	0.995	0.500	0.907	0.942	0.994	0.848	0.980	0.975	0.997
1	0.988	0.999	0.058	0.803	0.983	0.998	0.347	0.871	0.991	0.999
2	0.832	0.979	0.464	0.911	0.760	0.969	0.928	0.992	0.924	0.992
3	0.884	0.986	0.311	0.830	0.818	0.978	0.937	0.993	0.953	0.995
4	0.872	0.977	0.500	0.908	0.819	0.975	0.903	0.988	0.887	0.985
5	0.814	0.971	0.593	0.929	0.685	0.947	0.911	0.989	0.815	0.973
6	0.901	0.988	0.491	0.906	0.856	0.984	0.835	0.973	0.931	0.992
7	0.892	0.988	0.229	0.846	0.869	0.986	0.714	0.944	0.926	0.992
8	0.834	0.978	0.501	0.907	0.782	0.974	0.911	0.990	0.933	0.991
9	0.896	0.987	0.624	0.916	0.858	0.983	0.903	0.986	0.920	0.990

Table 2: MNIST $c = 0.1$

Normal class	NAE		DAGMM		DSEBMs		GeoTrans		RSRAE	
	AUC	AP	AUC	AP	AUC	AP	AUC	AP	AUC	AP
0	0.901	0.966	0.095	0.723	0.748	0.915	0.752	0.891	0.943	0.982
1	0.981	0.995	0.242	0.708	0.976	0.994	0.323	0.686	0.977	0.994
2	0.740	0.885	0.695	0.874	0.570	0.796	0.875	0.954	0.876	0.958
3	0.768	0.895	0.500	0.771	0.759	0.918	0.855	0.948	0.896	0.965
4	0.792	0.884	0.500	0.766	0.802	0.930	0.867	0.954	0.867	0.943
5	0.685	0.837	0.476	0.745	0.612	0.812	0.801	0.921	0.748	0.895
6	0.832	0.937	0.350	0.730	0.771	0.922	0.826	0.928	0.888	0.962
7	0.837	0.940	0.439	0.776	0.851	0.954	0.691	0.863	0.888	0.962
8	0.708	0.870	0.469	0.712	0.696	0.893	0.833	0.934	0.900	0.964
9	0.836	0.935	0.343	0.657	0.830	0.942	0.827	0.930	0.891	0.960

Table 3: MNIST $c = 0.3$

Normal class	NAE		DAGMM		DSEBMs		GeoTrans		RSRAE	
	AUC	AP	AUC	AP	AUC	AP	AUC	AP	AUC	AP
0	0.884	0.930	0.496	0.662	0.694	0.846	0.690	0.789	0.931	0.962
1	0.979	0.992	0.427	0.689	0.973	0.988	0.268	0.550	0.945	0.976
2	0.700	0.791	0.147	0.540	0.566	0.735	0.832	0.898	0.842	0.911
3	0.717	0.794	0.494	0.661	0.704	0.842	0.845	0.913	0.855	0.918
4	0.764	0.806	0.388	0.634	0.757	0.860	0.835	0.911	0.824	0.886
5	0.641	0.718	0.616	0.704	0.565	0.680	0.670	0.776	0.720	0.812
6	0.800	0.871	0.363	0.601	0.734	0.861	0.720	0.802	0.863	0.923
7	0.822	0.895	0.153	0.493	0.815	0.904	0.647	0.761	0.861	0.923
8	0.642	0.749	0.370	0.616	0.667	0.816	0.679	0.777	0.885	0.932
9	0.810	0.871	0.259	0.597	0.808	0.894	0.769	0.833	0.884	0.934

Table 4: MNIST $c = 0.5$

Normal class	NAE		DAGMM		DSEBMs		GeoTrans		RSRAE	
	AUC	AP	AUC	AP	AUC	AP	AUC	AP	AUC	AP
0	0.861	0.881	0.340	0.518	0.592	0.738	0.673	0.719	0.915	0.938
1	0.974	0.987	0.711	0.813	0.969	0.982	0.315	0.494	0.923	0.951
2	0.663	0.695	0.433	0.575	0.479	0.562	0.819	0.849	0.820	0.862
3	0.677	0.694	0.491	0.582	0.675	0.774	0.836	0.881	0.881	0.912
4	0.726	0.713	0.466	0.575	0.727	0.794	0.775	0.832	0.811	0.834
5	0.606	0.618	0.468	0.546	0.532	0.570	0.651	0.692	0.693	0.735
6	0.785	0.814	0.232	0.562	0.664	0.745	0.706	0.730	0.867	0.903
7	0.810	0.839	0.440	0.593	0.796	0.859	0.645	0.684	0.849	0.886
8	0.616	0.664	0.792	0.847	0.645	0.741	0.678	0.711	0.889	0.913
9	0.780	0.797	0.390	0.499	0.795	0.851	0.729	0.758	0.874	0.902

Table 5: MNIST $c = 0.7$

Normal class	NAE		DAGMM		DSEBMs		GeoTrans		RSRAE	
	AUC	AP	AUC	AP	AUC	AP	AUC	AP	AUC	AP
0	0.845	0.831	0.572	0.551	0.484	0.588	0.612	0.596	0.888	0.899
1	0.917	0.981	0.250	0.467	0.967	0.976	0.285	0.421	0.908	0.926
2	0.632	0.609	0.565	0.595	0.466	0.500	0.767	0.770	0.804	0.813
3	0.639	0.602	0.432	0.457	0.645	0.700	0.795	0.806	0.848	0.855
4	0.693	0.632	0.535	0.520	0.690	0.705	0.749	0.749	0.789	0.767
5	0.560	0.517	0.456	0.497	0.499	0.464	0.737	0.725	0.680	0.668
6	0.754	0.738	0.455	0.463	0.639	0.687	0.683	0.653	0.858	0.869
7	0.790	0.797	0.273	0.491	0.776	0.807	0.606	0.583	0.825	0.830
8	0.581	0.568	0.457	0.459	0.616	0.661	0.678	0.665	0.889	0.893
9	0.763	0.740	0.472	0.493	0.778	0.801	0.771	0.757	0.865	0.863

Table 6: MNIST $c = 0.9$

A.6. Detailed results for Fashion-MNIST in Section 5

The following tables report the AUC and AP scores of RSRAE and different benchmarks for Fashion-MNIST. Each table reports the results for a specific constant c , where c is approximate outlier ratio.

	NAE		DAGMM		DSEBMs		GeoTrans		RSRAE	
Normal class	AUC	AP	AUC	AP	AUC	AP	AUC	AP	AUC	AP
T-shirt/top	0.771	0.970	0.238	0.826	0.886	0.986	0.739	0.956	0.896	0.988
Trouser	0.918	0.991	0.413	0.898	0.976	0.998	0.612	0.919	0.937	0.993
Pullover	0.770	0.969	0.471	0.886	0.874	0.980	0.872	0.979	0.880	0.979
Dress	0.757	0.967	0.546	0.917	0.903	0.987	0.579	0.908	0.888	0.983
Coat	0.832	0.978	0.370	0.877	0.876	0.978	0.820	0.967	0.878	0.980
Sandals	0.148	0.793	0.868	0.975	0.839	0.975	0.913	0.990	0.424	0.870
Shirt	0.691	0.952	0.263	0.840	0.799	0.938	0.813	0.971	0.804	0.966
Sneaker	0.666	0.953	0.490	0.906	0.975	0.997	0.974	0.997	0.971	0.997
Bag	0.721	0.957	0.741	0.962	0.578	0.926	0.749	0.958	0.864	0.983
Ankle boot	0.867	0.983	0.085	0.793	0.969	0.997	0.971	0.997	0.986	0.999

Table 7: Fashion MNIST $c = 0.1$

	NAE		DAGMM		DSEBMs		GeoTrans		RSRAE	
Normal class	AUC	AP	AUC	AP	AUC	AP	AUC	AP	AUC	AP
T-shirt/top	0.724	0.906	0.500	0.769	0.879	0.956	0.680	0.834	0.873	0.959
Trouser	0.887	0.966	0.750	0.876	0.959	0.986	0.420	0.701	0.865	0.954
Pullover	0.716	0.896	0.341	0.662	0.835	0.937	0.793	0.899	0.862	0.934
Dress	0.689	0.887	0.500	0.769	0.873	0.945	0.494	0.741	0.847	0.945
Coat	0.809	0.933	0.519	0.762	0.877	0.946	0.733	0.870	0.879	0.949
Sandals	0.095	0.581	0.789	0.929	0.817	0.909	0.659	0.858	0.321	0.662
Shirt	0.625	0.849	0.500	0.769	0.766	0.909	0.712	0.885	0.767	0.888
Sneaker	0.533	0.782	0.437	0.700	0.969	0.989	0.796	0.893	0.696	0.851
Bag	0.633	0.839	0.500	0.769	0.573	0.796	0.623	0.844	0.804	0.925
Ankle boot	0.786	0.910	0.529	0.756	0.950	0.971	0.801	0.885	0.961	0.988

Table 8: Fashion MNIST $c = 0.3$

	NAE		DAGMM		DSEBMs		GeoTrans		RSRAE	
Normal class	AUC	AP	AUC	AP	AUC	AP	AUC	AP	AUC	AP
T-shirt/top	0.706	0.849	0.402	0.597	0.835	0.906	0.574	0.693	0.879	0.940
Trouser	0.875	0.941	0.363	0.554	0.953	0.973	0.626	0.722	0.862	0.924
Pullover	0.698	0.834	0.361	0.566	0.797	0.872	0.720	0.822	0.855	0.893
Dress	0.668	0.815	0.642	0.775	0.855	0.898	0.460	0.632	0.845	0.911
Coat	0.804	0.896	0.402	0.576	0.837	0.884	0.740	0.820	0.878	0.921
Sandals	0.077	0.465	0.732	0.838	0.785	0.813	0.835	0.899	0.223	0.509
Shirt	0.608	0.768	0.310	0.556	0.742	0.842	0.695	0.817	0.760	0.826
Sneaker	0.483	0.642	0.564	0.746	0.960	0.978	0.691	0.737	0.758	0.818
Bag	0.594	0.729	0.477	0.725	0.672	0.769	0.617	0.760	0.746	0.827
Ankle boot	0.752	0.827	0.216	0.501	0.947	0.973	0.734	0.770	0.858	0.926

Table 9: Fashion MNIST $c = 0.5$

	NAE		DAGMM		DSEBMs		GeoTrans		RSRAE	
Normal class	AUC	AP	AUC	AP	AUC	AP	AUC	AP	AUC	AP
T-shirt/top	0.695	0.797	0.357	0.473	0.812	0.851	0.578	0.616	0.865	0.907
Trouser	0.863	0.912	0.392	0.490	0.943	0.954	0.436	0.519	0.889	0.909
Pullover	0.689	0.777	0.506	0.550	0.773	0.821	0.768	0.783	0.850	0.851
Dress	0.652	0.742	0.259	0.439	0.810	0.806	0.437	0.529	0.801	0.837
Coat	0.796	0.855	0.482	0.524	0.753	0.756	0.682	0.719	0.882	0.898
Sandals	0.087	0.394	0.186	0.438	0.741	0.698	0.502	0.563	0.172	0.413
Shirt	0.601	0.695	0.328	0.475	0.741	0.788	0.681	0.758	0.761	0.776
Sneaker	0.471	0.544	0.769	0.793	0.937	0.950	0.577	0.583	0.809	0.843
Bag	0.570	0.627	0.232	0.445	0.603	0.643	0.573	0.674	0.707	0.723
Ankle boot	0.729	0.737	0.105	0.576	0.843	0.860	0.739	0.724	0.886	0.907

Table 10: Fashion MNIST $c = 0.7$

	NAE		DAGMM		DSEBMs		GeoTrans		RSRAE	
Normal class	AUC	AP	AUC	AP	AUC	AP	AUC	AP	AUC	AP
T-shirt/top	0.683	0.744	0.391	0.435	0.791	0.800	0.592	0.581	0.859	0.879
Trouser	0.855	0.883	0.568	0.547	0.911	0.886	0.489	0.499	0.789	0.774
Pullover	0.683	0.725	0.565	0.554	0.749	0.768	0.627	0.617	0.847	0.807
Dress	0.640	0.681	0.588	0.548	0.819	0.779	0.487	0.493	0.798	0.794
Coat	0.790	0.817	0.273	0.387	0.717	0.753	0.695	0.672	0.887	0.880
Sandals	0.080	0.340	0.916	0.907	0.721	0.626	0.658	0.658	0.147	0.352
Shirt	0.590	0.629	0.463	0.481	0.738	0.772	0.648	0.678	0.767	0.730
Sneaker	0.450	0.467	0.674	0.689	0.924	0.924	0.698	0.605	0.834	0.832
Bag	0.552	0.545	0.561	0.575	0.586	0.578	0.569	0.609	0.701	0.652
Ankle boot	0.708	0.658	0.847	0.872	0.838	0.845	0.783	0.715	0.893	0.896

Table 11: Fashion MNIST $c = 0.9$